Indian Journal of Chemical Technology
Vol. 23, May, 2016 pp. 179-186

Nonlinear approach to flow instability of the orifice-centerline liquid induced by bubble chain rising in shear-thinning fluids

Wenyuan Fan* & Xiaohong Yin
School of Chemistry and Chemical Engineering, Tianjin University of Technology, Tianjin 300384, China
E-mail: wyfan@tjut.edu.cn

Received 21 April 2014; accepted 27 May 2014

The flow characteristics of orifice-centerline liquid induced by bubble chain rising in carboxymethylcellulose (CMC) aqueous solution have been investigated using nonlinear analysis of the velocity measured by Laser Doppler Anemometry. Both axial and radial velocities are determined under various gas flow rates (Q_g), measurement heights (z) and mass concentrations. The results show that for low Q_g, z and dilute solution, the characteristic frequency of the power spectrum is consistent with bubbling frequency, with uniform elliptical shape of reconstructed phase space. Largest Lyapunov exponents λ_1 in radial direction is approximately 10 times that in the axial direction. Whereas for high Q_g, z and concentrated solution, power spectrums are of broad coverage within low frequency range, with the compressed phase portrait and the raised λ_1. Especially, the liquid motion has a special feature of binary fraction in the present experiment.

Keyword: Bubble, Chaotic approach, Flow characteristic, Fractal analysis, Shear-thinning

Bubbly flows in non-Newtonian fluids have been paid considerable attention owing to its inherent scientific interest and importance in industrial application[1,2]. In these typical equipments which employ bubbly flow, the behaviors of bubble formation and rising are frequently encountered and will cause marked change in the flow fields as well as bubble shape, velocity and track, consequently, leading to significant effect on the contact efficiency between gas liquid two-phase. Thus, adequate understanding of the flow characteristics of the fluids surrounding a generating and rising bubble is therefore essential in optimizing the design of the gas-liquid contact equipments as well as taking overall insight into the interaction mechanism of bubble chain.

Unlike lots of researches in Newtonian fluids[3], the reports about this topic in non-Newtonian fluids are still much less. The earlier investigations were mostly focused on the experimental measurement and correlation of the volume of the bubble[4]. Miyahara *et al.*[5] proposed a simple spherical model for bubble formation by analysis of the difference between two bubbling stages. Terasaka and Tsuge[6,7] investigated experimentally the various influences on bubble volume respectively. Li[8] and Li *et al.*[9] advanced a novel model to predict the instantaneous size, shape and frequency of generating bubble by considering the influence of in-line interactions between two consecutive bubbles. Favelukis and Albalak[10] put forward a dynamic-control spherical model for bubble growth. Martín *et al.*[11,12] studied the two stages of bubble formation in both Newtonian and non-Newtonian fluids. Fan *et al.*[13] applied laser image technique to disclose the impact of the solution properties, orifice diameter and gas flow rate on the bubble detachment volume. Recently, Vélez-Cordero and Zenit[14] devoted to the bubble cluster formation in power-law shear-thinning fluids.

Besides, the previous reports were always addressed to bubble wake formed behind the leading bubble and its effect on trailing bubble, as well as its difference from that in Newtonian fluids. A negative wake in non-Newtonian fluids was firstly observed by Hassager[15]. Subsequently, by means of LDA, Bisgaard and Hassager[16] concluded that a negative wake was induced by elasticity. This peculiar phenomenon has also been observed for spheres falling in viscoelastic liquids[17]. Furthermore, Frank and Li[18,19] found the coexistence of three distinct zones around bubbles rising in polyacrylamide (PAM) solutions: a central downward flow behind the bubble, a conical upward flow surrounding the negative wake zone, and an upward flow zone in front of the bubble. Sousa *et al.*[20] conducted experimentally the interaction between consecutive Taylor bubbles rising in non-Newtonian solutions via sets of laser diodes/photocells and Particle Image Velocimetry (PIV). According to Sousa, for the less concentrated CMC solutions, the interaction between Taylor bubbles was similar to that found in Newtonian fluids, and for the most concentrated CMC solution, a negative wake forms behind the Taylor bubbles. Lin and Lin[21] have investigated experimentally coalescence mechanism of in-line two-unequal bubbles rising in PAM solution using Particle Image Analyzer (PIA), and proposed that the acceleration of the trailing bubble to the leading one owes to the pushing force caused by the viscoelastic effect and the dragging force caused by the negative pressure as well as the shear-thinning effect. Fan *et al.*[22] focused on the interaction between two parallel rising bubbles by analyzing the velocity field around bubbles using PIV. Li *et al.*[23] studied the viscosity distribution of the liquid around a rising bubble in CMC aqueous solutions by PIV. Vélez-Cordero *et al.*[24] conducted different experimental setups to study the rise of single bubble, two parallel bubble chains and bubble swarms in an elastic fluid with nearly constant viscosity. From a viewpoint of turbulent kinetic energy (TKE), Li *et al.*[25] investigated the turbulent characteristic of fluid induced by a chain of bubbles rising in non-Newtonian fluids by using PIV. Most recently, Amirnia *et al.*[26] focused the difference of bubble velocity, shape and path between small bubble and larger bubble rising in xanthan gum and CMC fluids.

Nevertheless, a detailed liquid flow dynamics around a rising bubble is crucial to determine the mechanism of bubble-bubble interaction as well as coalescence during bubble ascension. Further, owing to several advantages[27], LDA has been one of the most favored tools for investigating the multiphase flow application. In this work, the dynamics of the flow field in front of the bubble rising in shear-thinning fluids will be investigated quantitatively by using both chaos and fractal theory.

Experimental Section

The experimental facility consisted of two parts: the bubble generation system and LDA measurement system as shown in Fig. 1. Bubble generation system included a Plexiglas square tank with dimensions of 15×15×50 cm (length×width×height), which was considered to be large enough and allow neglecting the effect of the wall on the shape and size of bubbles. A Plexiglas plate with dimension of 15.0×5.0×1.0 cm, having a polished orifice (inside diameter 2.0 mm) in its centre, was placed inside the tank 10 cm above the bottom for generating bubble. Stainless tubing with the inside diameter 2.0 mm linked the nitrogen cylinder, rotameter and orifices. Nitrogen pressure was maintained at little more than 0.1 MPa through adjusting a regulation valve, thus nitrogen bubbles are always generated synchronously at a stable frequency from the submerged orifice by adjusting the gas flow rate properly.

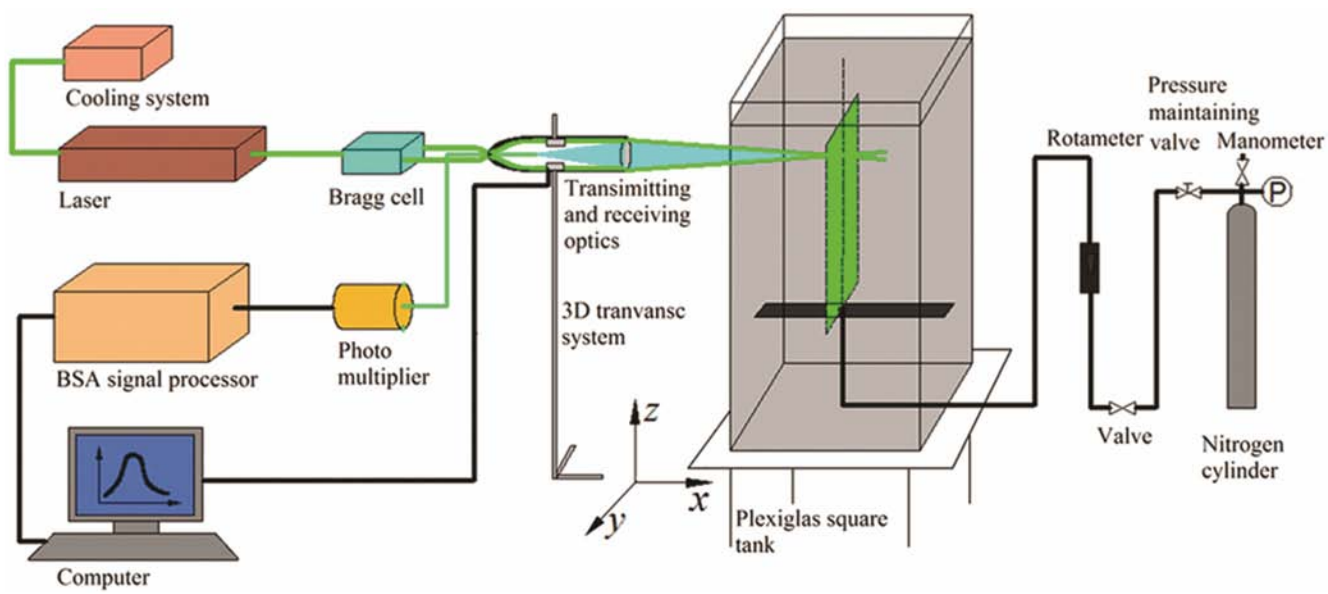

Fig. 1 — Schematic diagram of experimental system

LDA equipment (DANTEC, Fiber flow series 60X, Denmark) was applied and a PC using the Burst Spectrum Analyzer (BSA) Flow Software 2.1 for data acquisition. The backscattering mode in a cell-free system was used, and the vertical component was determined with green (λ= 514.5 nm) beams and the horizontal one with blue (λ= 488 nm) beams. The distilled water was used as a working solvent to avoid disturbance of the LDA system, and spherical glass particles of 10μm in diameter (density: 1.5×10^3 kg/m^3) were seeded and homogeneously distributed over the solution. These seeding particles carried by the liquid, reflected laser light toward the photo-detector probe and therefore, the liquid velocity was evaluated. Moreover, a pre-shift frequency of 40 kHz was utilized, and the time series obtained were 3 minutes long.

Experimental condition

The experimental conditions as follows: Gas flow rate (Q_g): 0.3, 0.5, 0.9×10^{-6} m^3·s^{-1}; measured height (z): 38.5, 48.5, 58.5, 68.5, 78.5×10^{-3} m. Two kinds of solutions were employed in this work: 0.15% CMC in water (wt%), marked as CMC(1), and 0.15% CMC in a mixture of 76.9-23.1% water-glycerol, marked as CMC(2). The physical properties of rheological characteristics of CMC aqueous solutions were measured by Rheometer of StressTech (REOLOGICA Instruments AB, Sweden), and the results show that the behavior of shear-thinning of the fluid can be described very well by Carreau model (Eq. (1)) within shear rate range from 2.0 to 60 s^{-1}. The results were summarized in Table 1.

$$\frac{\ -\ _{\infty}}{_{0}-\ _{\infty}}=\left[1+(\ \ \dot{}\ )^{2}\right]^{(n-1)/2} \quad \ldots(1)$$

where, $_0$, $_\infty$, and n are zero-shear viscosity, infinite shear viscosity, time constant and flow index respectively.

Results and Discussion

The instantaneous velocities are stochastic signals with time interval because LDA measurement is random in time and has a signal only when seeding particle passes through the measured point.

Table 1—Rheological parameters of non-Newtonian CMC solutions

Fluids	$_0$/Pa·s	$_\infty$/Pa·s	/s	n
0.15%CMC(1)	0.03762	0.001	0.068962	0.80767
0.15%CMC(2)	0.08282	0.001	0.101070	0.73567

Accordingly, linear interpolation of the data is necessary before time-frequency analysis of velocity. The interpolated time series of axial velocity fluctuates around a certain value of average-velocity.

Power spectrum

Information of bubble motion can be obtained through analysis of liquid flow feature using time-frequency technology. Here, as one of the qualitative methods, Fourier analysis method is adopted by calculating turbulent power spectrum of the liquid velocity signal $w(t)$. Discrete Fourier Transform (DFT) of the signal $w(t)$ can be expressed as following:

$$W(f)=\sum_{t=0}^{N-1} w(t)\mathrm{e}^{-i2\ \ tf/N} \quad \ldots(2)$$

The power spectrum of the signal can then be calculated by

$$P(f)=\left|W(f)\right|^{2} \quad \ldots(3)$$

In present experiments, the single bubble rose up straightly without any obvious swinging, and also its shape became symmetric with the axis of the vertical line passing through orifice centre, so the measured domain was defined along the center line of bubble rising channel (i.e. y=0). Figure 2 presents the power spectrum derived from both axial and radial velocity time series for various conditions respectively. It is demonstrated that for z = 53.5×10^{-3} m, the both power spectrums corresponding to the radial velocities exhibits only one major peak, which is consistent with the bubble periodic injection frequency (2.2 Hz), as shown in Fig. 2a. While for z = 78.5×10^{-3} m, bubble accelerated velocity results in a strong bubble-bubble interaction. Accordingly, characteristic frequency of velocity drops slightly to 2.1 and meanwhile several small peaks appear due to the accelerated liquid turbulence, which is caused by the decrease of fluid viscosity owing to its shear-thinning effect, as shown in Fig. 2b. By contrast, the power spectrum in CMC(2) solution has been covered by broad peaks in low frequency, implying its involvement of large energy. Generally, the low-frequency region corresponds to the large-scale vortex, produced gradually by the enhancement of the liquid viscosity. But for z = 78.5×10^{-3} m, the characteristic peak at frequency (3.2 Hz) disappears gradually, while a spacious large-area peak with a larger magnitude

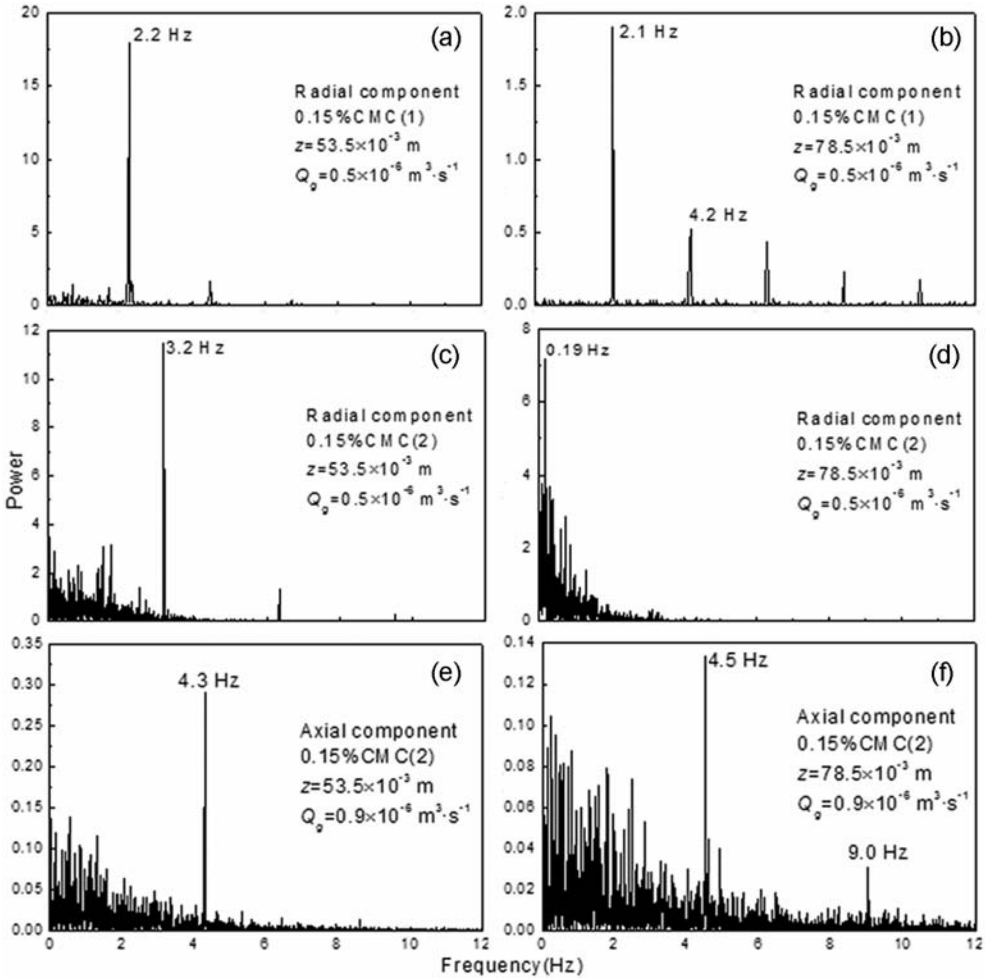

Fig. 2 — Power spectrums of velocities under various conditions

occurs. It reveals that large-scale fluctuation in both axial and radial velocities is reinforced. Moreover, a low-frequency characteristic peak (0.19 Hz) in radial velocity arises, which can be attributed to the liquid vibration in the region studied, as shown in Fig. 2 (c) and (d).

As the gas flow rate adds up to $Q_g = 0.9 \times 10^{-6}$ $m^3 \cdot s^{-1}$, the magnitudes of axial characteristic peaks for $z = 53.5\times10^{-3}$ m and $z = 78.5\times10^{-3}$ m increase to 4.3 Hz and 4.5 Hz respectively, which is consistent with the continuous bubble forming and rising frequency. Similarly, there exist numerous irregular broad peaks in the low-frequency region. However, the large-scale turbulent intensity surrounding the rising bubble is enhanced by increasing bubble velocity, and consequently, the magnitudes of radial characteristic peaks in power spectrum start to decline, as shown in Fig. 2 (e) and (f).

Phase space reconstruction

Nearly all methods of nonlinear analysis of signals are based on the reconstruction of an attractor of the dynamic evolution of the system in phase space. Here, Takens' embedding theorem is employed to reconstruct attractors[28]. A set of time series data of velocity fluctuations is utilized to generate a *m*-dimensional state vector. For a measured scalar time series signal $\{ x_1, x_2, \ldots, x_{n-1}, x_n, \ldots \}$, $X(i)$ is a *m*-dimensional reconstructive vector given by

$$X(i) = \left[x(i), x(i+\ ), x(i+2\ ), \ldots, x\left(i+(m-1)\ \right) \right], i = 1, 2, \ldots \quad (4)$$

where τ is the delay time, m is embedding dimension.

Figure 3 presents two typical examples of 2-dimensional phase portraits of reconstructed phase space of axial-velocity time series. It is found that the velocity signals is always limited to a certain area,

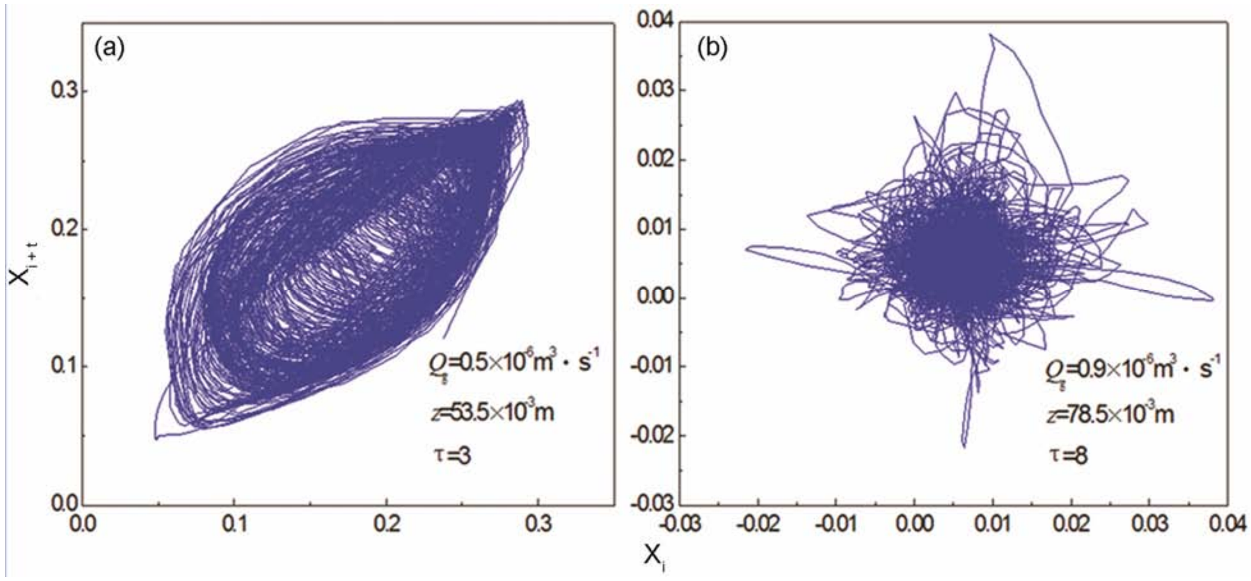

Fig. 3 — Phase portrait of reconstructed phase space

and for low z and Q_g, the phase portrait take on uniform elliptical shape due to periodic liquid motion induced by periodic bubble rising in the position involved, as shown in Fig. 3a. However for $z = 78.5 \times 10^{-3}$ m and $Q_g = 0.9 \times 10^{-6}$ m^3·s^{-1}, the bubble rising velocity increases obviously, hence the liquid turbulence is intensified and large-scale turbulent intensity around bubble increases, consequently, leading to significant compression of phase portrait, as shown in Fig. 3b. Especially, all the trajectories in both phase portraits, corresponding to certain independent frequencies, are never repeated with their own complex shape. It reveals that the system instability compels state trajectories to extend infinitely, with their dense but ergodic tracks in phase space. On the other hand, the system stable factors, however, confines the trajectories to a definite space, forming a hierarchical chaotic attractor with the obvious features of the extension.

Hurst exponent

As a classic calculated method in fractal theory, the rescale-range (R/S) analysis with the determination of the Hurst exponent H has successfully been applied for pressure fluctuation signals in fluidization[29] and for optical transmittance probe signals[30]. When a positive correlation exists in the time-series data, H can vary from 0.5 to 1.0. Highest values of H indicate that the studied signal is persistent, which means that the process exhibits long-term tendencies. When the value of H is from zero to 0.5, the signal is negatively correlated and for the lowest values of H, the signal becomes anti-persistent. When for H≈0.5, the system is stochastic.

For any delay n ($n \le N$) in time series $\{x_i\}, i = 1, 2, \ldots, N$, the accumulative departure $X_{i,n}$ is calculated:

$$X_{i,n} = \sum_{k=1}^{i} (x_k - \bar{x}) \qquad \ldots (5)$$

where $\bar{x} = \frac{1}{n}\sum_{i=1}^{n} x_i$.

Then, the sample rescale range, R_n, and the mean square-root deviation of time series, S_n, are defined by

$$R_n = \max_{1\le i\le n} X_{i,n} - \min_{1\le i\le n} X_{i,n} \qquad \ldots (6)$$

$$S_n = \left[\frac{1}{n}\sum_{i=1}^{n} (x_i - \bar{x})^2\right]^{\frac{1}{2}} \qquad \ldots (7)$$

Hurst exponent (H) can be empirically determined by

$$R_n / S_n = (n/2)^H \qquad \ldots (8)$$

Finally, Hurst exponent is obtained by linear fitting the curve ln(R_n/S_n) vs. ln(n/2).

In this paper, there always exist two linear relationships in all the curves of ln(R/S)~ln(n), indicating that the liquids motion in the rising channel center during bubble rise in non-Newtonian fluids has two different dynamic characteristics. Typical calculated results of the Hurst exponent for both axial and radial velocity time series are shown in Fig. 4.

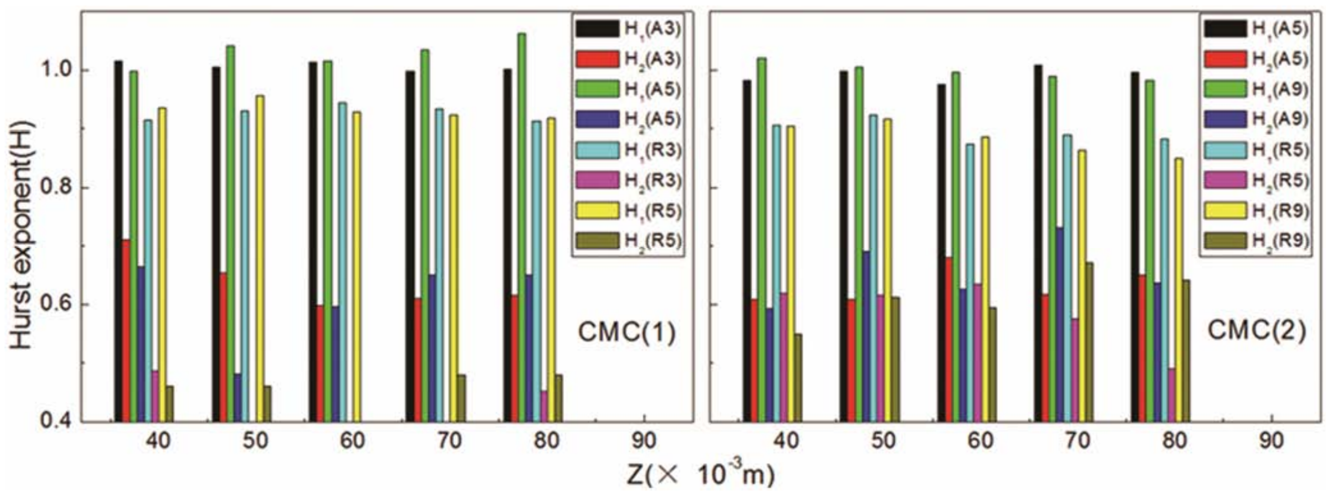

Fig. 4 — Hurst exponent versus measured height in 0.15%CMC (1) and 0.15%CMC (2). A and R denote axial and radial directions; 3, 5 and 9 denote respectively 0.3, 0.5 and 0.9×10^{-6} $m^3\cdot s^{-1}$

It can be seen that all signals at the measured points take on binary fractal features: For a minor time delay, the values of Hurst exponent H_1, larger than 0.85, exhibit positive persistence. This persistence implies that a given positive increment of liquid pulse signal in the past will lead to an average positive increment of the signal in a certain period of in the future. However, this persistence works only within a certain range. With the increase of the delay *n*, the values of Hurst exponents H_2 derived from the most signals begin to reduce to a small range(0.50~0.74), which suggests that positive persistence in the system starts to weaken steadily. Furthermore, some values of H_2 are less than 0.5, revealing the anti-persistence feature. This signifies the complex nature of the liquid motion induced by bubble rising in non-Newtonian fluids under the experimental gas flow rate.

Largest Lyapunov exponents

Largest Lyapunov exponent, the average rates of divergence or convergence of nearby orbits in independent phase space, has been employed to describe the local instability of chaotic orbits and has been the quantitative criterion of chaotic orbits for the sensitive dependence on initial conditions. Once the optimal delay time τ and the minimum embedding dimension *m* were determined, the Lyapunov exponent could be calculated by using Wolf method[31] after pretreatment of noise reduction of time series.

For the measured data in the form of time series:

$$X_i\left(m+1\right)=\left(x_i, x_{i+}\ ,\ldots, x_{i+m}\ \right) \qquad \ldots (9)$$

In the attractor immersed in *D* dimensional space, two closest points situating at a distance of at least one orbiting period one from another, are selected. The distance between the points as well as the distance after the passage of some evolution time are represented by $L(t_j)$ and $L(t_{j+1})$. The largest Lyapunov exponent is calculated according to the formula:

$${}_1=\frac{1}{t}\sum_{i=0}^{m}\ln\frac{L(t_{i+1})}{L(t_i)} \qquad \ldots (10)$$

where *m* is the number of point pairs examined, *t* the time of evolution.

Figure 5 indicates that largest Lyapunov exponents λ_1 in axial and radial directions vary with the measured height under various gas flow rates and CMC solutions concentration. The computed values of λ_1(0~1.0) imply chaotic motion nature of the liquid within the centre of bubble rising channel. For $z = 38.5\times10^{-3}$ m, $Q_g = 0.3\times10^{-6}$ $m^3\cdot s^{-1}$ and 0.15% CMC (1), the λ_1 in axial direction becomes close to zero, corresponding to the periodic motion of fluids with low viscosity. However, the λ_1 in radial direction is approximately 10 times that in the axial direction under the same conditions, illustrating that radial motion of channel center fluid begins to deviate heavily from periodic pattern. Further, by comparing the λ_1 for $Q_g = 0.3\times10^{-6}$ $m^3\cdot s^{-1}$ with that for $Q_g = 0.5\times10^{-6}$ $m^3\cdot s^{-1}$, it is shown that the λ_1 rises with

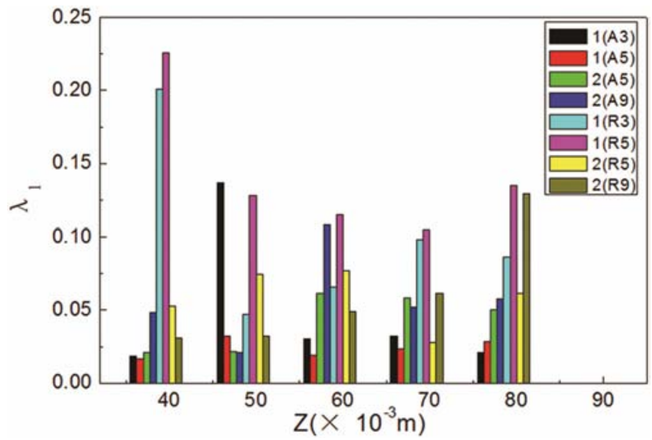

Fig. 5 — Largest Lyapunov exponent versus measured height. 1 and 2 denote CMC(1) and CMC(2); A and R denote axial and radial directions; 3, 5 and 9 denote respectively 0.3, 0.5 and $0.9{\times}10^{-6}$ $m^3{\cdot}s^{-1}$

the gas flow rate, which suggests that under high gas flow rate, the dynamics of liquid radial movement become more complex, i. e. system chaotic degree increases gradually. Furthermore, for $Q_g = 0.9 \times 10^{-6}$ $m^3{\cdot}s^{-1}$ and 0.15% CMC (2), the λ_1 in radial direction increases with the measured height. This can be explained as follows: The deduce of solution viscosity leads to the slight in-line interaction between two successive bubbles in the measured position, and the weak interplay at low position keeps bubble a quasi-periodic ascending state, consequently, resulting in small λ_1. Whereas for the high position, the in-line interaction between bubbles will enhance due to the intensification of compression movement of bubbles coupled with the shear-thinning effect of CMC solution. Hence, for large height condition, the motion of CMC solution in the channel center deviates heavily from periodic pattern, causing large λ_1.

Conclusion

The Laser Doppler anemometry has been applied to measure the liquid instant velocities induced by a bubble chain rising in non-Newtonian CMC fluids under various experimental conditions. The bubble dynamics in rising channel center are investigated by analysis the liquid velocity using chaos theory.

For low z, Q_g and dilute solution, the characteristic frequency of the power spectrum in axial and radial velocities is found to be consistent with bubble periodic shear frequency. Phase portrait takes on a uniform elliptical shape due to the results of liquid periodic motion caused by bubble periodic rising in the channel center. The λ_1 range from zero to 1.0, implies chaotic motion nature of the liquid within the center of the rising channel. Nonetheless, the λ_1 in radial direction is about 10 times that in the axial direction which indicates that radial motion of channel center fluid begins to deviate heavily from periodic pattern.

For high z, Q_g and concentrated solution, the in-line interaction between bubbles will enhance due to the intensification of compression movement of bubbles coupled with the shear-thinning effect of CMC solution. Therefore, both axial and radial power spectrums are of broad coverage within low frequency range, phase portrait is significantly compressed, and the λ_1 increases with the rise of system chaotic degree.

The results of fractal analysis show that the liquid motion has a unique feature of the binary fraction, and shows strong positive persistence characteristics for a small delay, but this positive persistence characteristic begins to decrease obviously with the delay increase.

Acknowledgement

Authors wish express their appreciation for the financial support by the National Natural Science Foundation of China (21106106, 21576214), and Tianjin Natural Science Foundation of China (12JCQNJC03700).

Nomenclature

D	=	phase space dimension
f	=	frequency, Hz
H	=	Hurst exponent
i	=	the ith measured point
$L(t_i)$	=	the distance of the ith couple nearest position after t time steps
m	=	embedded dimension; number of point pairs
n	=	time delay, s; number of signals in time series; parameter in Carreau model
N	=	sample number of data points in the time series; length of reconstructive vector X_i
$N_{i,n}$	=	cumulative deviation from the mean of a time series x_i in time delay n, $m{\cdot}s^{-1}$
P	=	power spectrum function
Q_g	=	gas flow rate, $m^3{\cdot}s^{-1}$
R_n	=	range function
S_n	=	rescale range function

t = time, time of evolution, s
w = liquid velocity signal, m·s^{-1}
W = function of discrete Fourier transform
x = measured liquid velocity time series, m·s^{-1}
X = reconstructive vector
y, z = *y* and *z* coordinates, m

Greek Symbols

$_0$ = zero-shear viscosity, Pa·s
$_\infty$ = infinite-shear viscosity, Pa·s
= Carreau model parameter, s; wavelength, m
$_1$ = largest Lyapunov exponents, bits·s^{-1}
= time delay, s

References

1 Shah Y T, Kelkar B G, Godbole S P & Deckwer W D, *AIChE J*, 28 (3) (1982) 353.
2 Kilonzo P M & Margaritis A, *Biochem Eng J*, 17 (1) (2004) 27.
3 Kulkarni A A & Joshi J B, *Ind Eng Chem Res*, 44 (2005) 5873.
4 Acharya A, Mashelkar R A & Ulbrecht J J, *Ind Eng Chem Fundamen*, 17 (1978) 230.
5 Miyahara T, Wang W H & Takahashi T, *J Chem Eng Japan*, 21 (6) (1988) 620.
6 Terasaka K & Tsuge H, *AIChE J*, 43 (11) (1997) 2903.
7 Terasaka K & Tsuge H, *Chem Eng Sci*, 56 (10) (2001) 3237.
8 Li H Z, *Chem Eng Sci*, 54 (13-14) (1999) 2247.
9 Li H Z, Mouline Y & Midoux N, *Chem Eng Sci*, 57 (3) (2002) 339.
10 Favelukis M & Albalak R J, *Chem Eng J Biochem Eng J*, 63 (3) (1996) 149.
11 Martín M, Montes F J & Galán M A, *Chem Eng Sci*, 61 (2) (2006) 363.
12 Martín M, Montes F J & Galán M A, *Chem Eng Sci*, 61 (16) (2006) 5196.
13 Fan W Y, Jiang S K, Zhu C Y, Ma Y G & Li H Z, *Opt Laser Technol*, 40 (2) (2008) 389.
14 Vélez-Cordero J R & Zenit R, *J Non-Newton Fluid Mech*, 166 (1-2) (2011) 32.
15 Hassager O, *Nature*, 279 (1979) 402.
16 Bisgaard C & Hassager O, *Rheol. Acta*, 21 (1982) 537.
17 Arigo M T & McKinley G H, *Rheol. Acta*, 37 (1998) 307.
18 Frank X & Li H Z, *Phys Rev E*, 71 (2005) 036309.
19 Frank X & Li H Z, *Phys Rev E*, 74 (2006) 056307.
20 Sousa R G, Pinto A M F R & Campos J B L M, *Int J Multiphase Flow*, 33 (9) (2007) 970.
21 Lin T J & Lin G M, *Chem Eng J*, 155 (2009) 750.
22 Fan W Y, Ma Y G, Li X L & Li H Z, *Chin J Chem Eng*, 17 (2009) 904.
23 Li S B, Ma Y G, Fu T T, Zhu C Y & Li H Z, *Braz J Chem Eng*, 29 (2) (2012) 265.
24 Vélez-Cordero J R, Sámano D & Zenit R, *J Non-Newtonian Fluid Mech*, 175-176 (2012) 1.
25 Li S B, Ma Y G, Zhu C Y, Fu T T, & Li H Z, *Chin J Chem Eng*, 20 (5) (2012) 883.
26 Amirnia S, de Bruyn J R, Bergougnou M A & Margaritis A, *Chem Eng Sci*, 94 (2013) 60.
27 Kumara W A S, Elseth G, Halvorsen B M & Melaaen M C, *Flow Meas Instrum*, 21(2) (2010) 105.
28 Takens F, *Detecting strange attractors in Turbulence, Lecture Notes in Mathematics* (Springer Verlag, Berlin), 1981.
29 Drahos J, Bradka F & Puncochar M, *Chem Eng Sci*, 47 (1992) 4069.
30 Kikuchi R, Yano T, Tsutsumi A, Yoshida K, Punchochar M & Drahos J, *Chem Eng Sci*, 52 (1997) 3741.
31 Wolf A, Swift J B, Swinney H L & Vastano J A, *Physica*, 16 (1985) 285.